ELSEVIER

Journal of Nuclear Materials 297 (2001) 89–96

journal of nuclear materials

www.elsevier.com/locate/jnucmat

Radiation damage and nanocrystal formation in uranium–niobium titanates

J. Lian, S.X. Wang [1], L.M. Wang, R.C. Ewing *

Department of Nuclear Engineering and Radiological Sciences, University of Michigan, Ann Arbor, MI 48109-2104, USA

Received 28 November 2000; accepted 27 March 2001

Abstract

Two uranium–niobium titanates, $U_{2.25}Nb_{1.90}Ti_{0.32}O_{9.8}$ and $Nb_{2.75}U_{1.20}Ti_{0.36}O_{10}$, formed during the synthesis of brannnerite (UTi_2O_6), a minor phase in titanate-based ceramics investigated for plutonium immobilization. These uranium titanates were subjected to 800 keV Kr^{2+} irradiation from 30 to 973 K. The critical amorphization dose of the U-rich and Nb-rich titanates at room temperature were 4.72×10^{17} and 5×10^{17} ions/m^2, respectively. At elevated temperature, the critical amorphization dose increases due to dynamic thermal annealing. The critical amorphization temperature for both Nb-rich and U-rich titanates is ~933 K under a 800 keV Kr^{2+} irradiation. Above the critical amorphization temperature, nanocrystals with an average size of ~15 nm were observed. The formation of nanocrystals is due to epitaxial recrystallization. At higher temperatures, an ion irradiation-induced nucleation-growth mechanism also contributes to the formation of nanocrystals.

1. Introduction

Pyrochlore (e.g., $Gd_2Ti_2O_7$) is an actinide host phase proposed for the immobilization of high level wastes and excess weapon plutonium, and a pyrochlore-rich (95%) ceramic with 5% $(Ti_{0.9}Hf_{0.1})O_2$ is being investigated by the US Department of Energy (DOE) as the baseline titanate ceramic for the immobilization of plutonium [1–6]. Pyrochlore, $A_{1-2}B_2O_6(O, OH)_{0-1}$, is a derivative of the fluorite structure with one-eighth fewer anions and two cation sites. Synthetic pyrochlore has a great variety of chemical compositions due to substitutions at the A and B sites. Over 450 synthetic pyrochlores have been synthesized with this structure type [7], and many actinide compositions are possible [8]. Researchers at Australian Nuclear Science and Technology Organisation (ANSTO) have demonstrated Pu incorporation in zirconolite-rich and zirconolite/pyrochlore titanate ceramics [9,10]. Radiation effects in pyrochlore-based titanate ceramics have been extensively studied [2,11–16].

However, during the synthesis of pyrochlore, other complex titanate phases form. For example, the mineral brannerite (UTi_2O_6), which contains Gd, Hf and Th, is a minor phase associated with synthetic pyrochlore [9,17]. Natural brannerite is metamict (amorphous) as a result of the α-decay of the constituent radionuclides U, Th and their daughter products. There are a number of elemental substitutions for both uranium (Pb, Ca, Th, Y and Ce) and titanium (Si, Al, Fe) [18,19]. Gd- and Ca-containing brannerite have been synthesized, and other atomic-scale substitutions (e.g., Nb, Fe, Zr and Pu) in brannerite have also been explored [20]. The high U-content of brannerite (up to 62.8 wt%) and its potential as the nuclear waste form for the immobilization of actinides have emphasized the importance of radiation damage effects in these titanate phases [21,22]. Radiation effects on synthetic brannerite structure-types have been studied by ion beam irradiation and temperature dependence has been determined [22,23].

The minor titanate phases may also incorporate Pu and actinides, and their response to radiation damage must be evaluated. Radiation damage in two complex uranium–niobium titanates that formed during the synthesis of brannerite has been studied by ion beam

* Corresponding author. Tel.: +1-734 647 8529; fax: +1-734 647 8531.

E-mail address: rodewing@umich.edu (R.C. Ewing).

[1] Present address: Micron Technology Inc., Mail stop 632, Boise, ID 83707, USA.

0022-3115/01/$ - see front matter
PII: S0022-3115(01)00585-2

irradiation, and the radiation effects were observed by in situ transmission electron microscopy (TEM).

2. Experimental

The material was prepared from Nb_2O_5, a mixture of aqueous uranyl nitrate and isopropyl titanate by an alkoxide/nitrate route. These were mixed thoroughly, dried, and calcined at 750°C and sintered at 1300°C under an argon atmosphere after pelletizing. TEM samples were prepared by mechanical polishing followed by ion milling under 4 keV argon ions. Selected area electron diffraction (SAD) and energy dispersive spectroscopy (EDS) in the TEM were used to identify the phases. X-ray diffraction (XRD) of the bulk samples was completed using a Rigaku diffractometer. A detailed chemical analysis was obtained by electron microprobe analysis (EMPA). The standards for Nb, U and Ti were pure Nb, UO_2 and TiO_2, respectively. The ZAF correction procedure was used for the quantitative analysis, and oxygen was estimated by stoichiometry.

In situ TEM was performed during a 800 keV Kr^{2+} irradiation from 30 to 973 K using the IVEM-Tandem Facility at Argonne National Laboratory. The radiation damage was simulated using TRIM-96 assuming a displacement energy (E_d) of 25 eV. The results showed that most of the 800 keV Kr^{2+} ions penetrated the sample thickness of the TEM observation, and the amount of implanted Kr^{2+} was negligible. The ion beam was aligned approximately normal to sample surface, and the dose rate was 6.25×10^{15} ions/m^2/s. In order to reduce beam heating at low temperatures, the dose rate at 30 K was decreased to 1.25×10^{15} ions/m^2/s. Structural changes were monitored by observing the selected area diffraction (SAD) pattern during irradiation. When all diffraction maxima disappeared and the diffraction pattern showed only the diffuse diffraction haloes, this ion dose was defined as the critical amorphization dose [24]. Because of the complex multi-phase nature of the synthetic material, and the fact that these phases have a similar morphology and structure, samples were mapped by EDS before ion irradiation. The mapped grains of the different phases were monitored during ion irradiation to ascertain the radiation resistance of the different phases. Ex situ high-resolution TEM (HRTEM) images of the radiation damage effects were acquired using a JEM 4000 EX electron microscope.

3. Results and discussion

3.1. Material characterization

The U–Nb titanate consisted of grains of several μm (Fig. 1(a)). A back-scattered electron image of the synthetic U–Nb titanate is shown in Fig. 1(b). Three phases coexist in this sample. EDS spectra indicate these phases are U-rich (a), Nb-rich (b) and Ti-rich (c), respectively. The compositions of the three phases were determined by EMPA to be $U_{2.25}Nb_{1.90}Ti_{0.32}O_{9.8}$, $Nb_{2.75}U_{1.20}Ti_{0.36}O_{10}$ and TiO_2, respectively. Fig. 2 shows an XRD pattern of the bulk sample. $U_3NbO_{9.8}$ (U-rich), UNb_3O_{10} (Nb-rich) and rutile were identified. The SAD patterns from Nb-rich phase match the XRD data for bulk UNb_3O_{10}.

UNb_3O_{10} is orthorhombic with $a = 1.277$, $b = 0.7369$, $c = 1.598$ nm [25]. The structure of UNb_3O_{10} is isostructural to the oxides of UM_3O_{10} (M = V, Ta); and two pseudo-hexagonal subcells ($a/b = \sqrt{3}$), containing one U or M atom, are found in the orthorhombic unit cell. For UV_3O_{10}, $a = 1.20$, $b = 0.6925$, $c = 1.619$ nm. The constants of the pseudo-hexagonal subcell are $a = 0.3463$ and $c = 0.405$ nm. The b dimension of orthorhombic cell of UV_3O_{10} is the result of alternating U- and V-subcells. The alternation of four layers of subcells along the c-axis leads to the degradation of the symmetry to the orthorhombic structure (*Fddd*) [26].

There are no structural data available for $U_3NbO_{9.8}$. However, $U_3NbO_{9.8}$ has an XRD pattern similar to that of UNb_3O_{10} [27,28]. As shown in Fig. 2, the strong

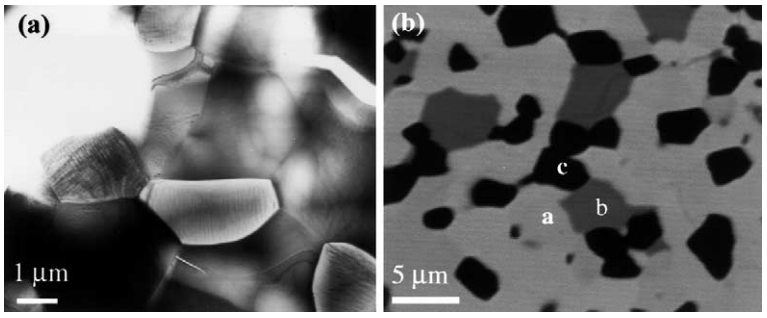

Fig. 1. (a) Bright-field TEM image of the U–Nb titanate showing grains of several μm; (b) Back-scattered electron image of synthetic uranium–niobium titanates: U-rich (a); Nb-rich (b) and Ti-rich phase (c).

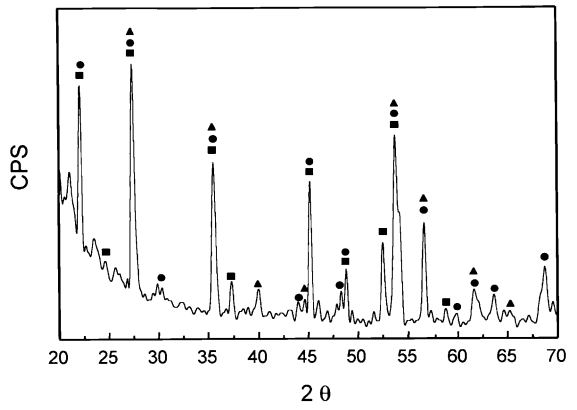

Fig. 2. XRD pattern showing the coexistence of three phases: (▲) TiO_2, (●) $U_3NbO_{9.8}$ and (■) UNb_3O_{10}.

diffraction peaks of the U-rich titanate overlap with the intense peaks of UNb_3O_{10}. Furthermore, the SAD pattern from the U-rich phase can be indexed using the crystal data of UNb_3O_{10}. A previous study [29] has indicated that the same type of superstructure for UM_3O_{10} (M = Nb, V, Ta) is found for some compounds with the composition U_3MO_{10}. Therefore, $U_3NbO_{9.8}$ may be isostructural to UNb_3O_{10} but with different site occupancies for U and Nb.

3.2. Susceptibility to ion irradiation-induced amorphization

A sequence of SAD patterns of the U-rich titanate irradiated by 800 keV Kr^{2+} at room temperature is shown in Fig. 3. Before irradiation, a diffraction pattern of a crystalline material was obtained (Fig. 3(a)). With an increase in ion dose, diffuse diffraction haloes appeared, and the intensity of diffraction maxima from the crystalline phase decreased (Figs. 3(b) and (c)). When the ion dose exceeded 4.72×10^{17} ions/m^2 (around 0.11 dpa based on the TRIM-96 calculation assuming a displacement energy, E_d, of 25 eV), the Bragg-diffraction maxima had completely disappeared, and the U-rich titanate was completely electron-diffraction amorphous (Fig. 3(d)). The ion irradiation-induced amorphization of the Nb-rich titanate was similar to that of the U-rich titanate. The critical amorphization dose (D_c) at room temperature for the Nb-rich titanate was 5×10^{17} ions/m^2. Within the uncertainty of experiments resulting from variations in sample thickness and orientation, no significant difference of critical amorphization dose was observed between the U-rich titanate and the Nb-rich titanate. The crystalline-to-amorphous transformation was also examined by HRTEM (Fig. 4). Before irradiation (Fig. 4(a)), the sample was crystalline. After a dose of 2.5×10^{17} ions/m^2, the crystalline structure was disrupted and mottled contrast in small areas was observed (Fig. 4(b)). With an increase in ion dose, the continuity of crystalline structure was gradually destroyed, and the fraction of amorphous volume increased. At an ion dose of 3.75×10^{17} ions/m^2, only isolated islands of crystallinity were observed (Fig. 4(c)). The critical amorphization dose was 4.72×10^{17} ions/m^2, and there was no evidence of remaining crystallinity (Fig. 4(d)).

Irradiation-induced amorphization is a complicated multi-stage process. Different models of mechanism have been proposed to describe the amorphization process [30]. Amorphization may occur when the accumulation of defects, created by ion irradiation, exceeds a critical concentration necessary for amorphization due to the overlap of collision cascades [31–33]. In the case of the direct-impact process [31,34], each incident energetic ion creates a cascade, a highly disordered volume, within 10^{-13} s. The cascade quenches rapidly and returns to the solid-state after tens of picoseconds. Depending on the kinetics of cascade and defect annealing, an amorphous core may remain within a cascade. The accumulation of these small amorphous volumes at a high enough ion dose eventually leads to the amorphization of the entire volume of the crystalline phase [30,34–36].

The temperature dependence of the critical amorphization dose is shown in Fig. 5. The temperature dependence curve was constructed by combining the experimental data of both U-rich and Nb-rich titanate phases. The critical amorphization dose required for full amorphization increases with temperature due to dynamic annealing. When the temperature is increased from 913 to 933 K, complete amorphization does not

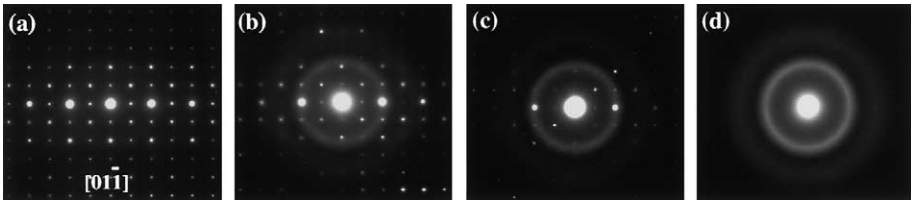

Fig. 3. A sequence of SAD patterns of the U-rich titanate irradiated by 800 keV Kr^{2+} at room temperature with different doses: (a) original; (b) 1.875×10^{17} ions/m^2; (c) 3.75×10^{17} ions/m^2 and (d) 4.72×10^{17} ions/m^2.

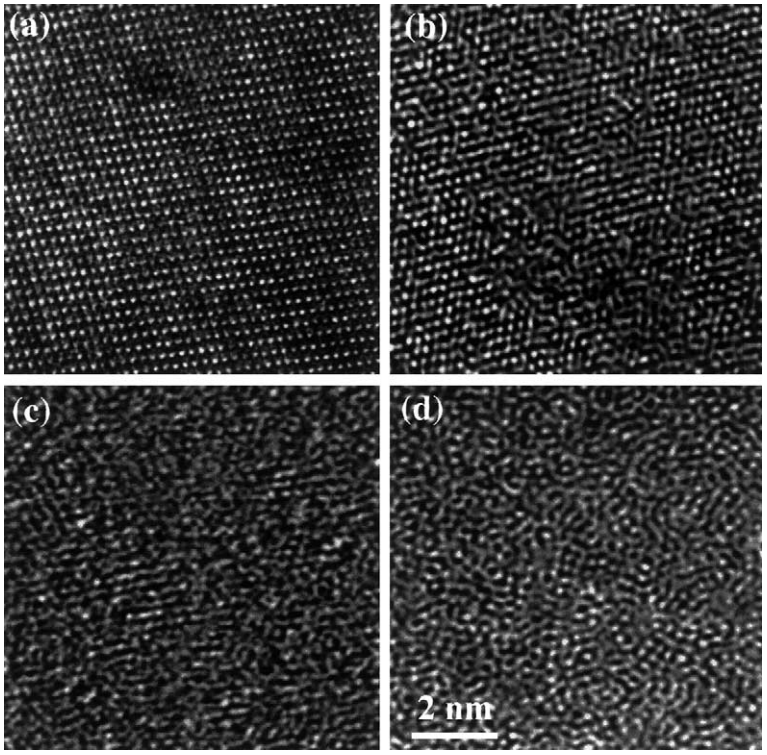

Fig. 4. HRTEM images of the U-rich phase irradiated by 800 keV Kr^{2+} at different doses: (a) before irradiation; (b) 1.875×10^{17}; (c) 3.75×10^{17} and (d) 4.72×10^{17} ions/m^2.

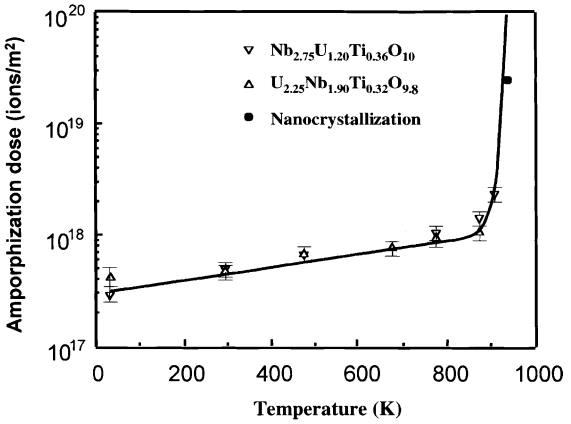

Fig. 5. Temperature dependence of critical amorphization dose of the U-rich and Nb-rich titanates irradiated by 800 keV Kr^{2+}. The black dot represents the point at which nanocrystals form at ~933 K.

occur. The critical amorphization temperature for both the U-rich and Nb-rich titanates irradiated by 800 keV Kr^{2+} ions is ~930 K. Based on the critical amorphization temperature, U-rich and Nb-rich titanates, present as trace components in the synthetic brannerite, are sensitive to the radiation damage at repository temperatures (300 to 500 K) and have a radiation damage susceptibility similar to that of the $Gd_2Ti_2O_7$ pyrochlore and $U_2Ti_2O_6$ brannerite [23]. The critical amorphization dose of $Gd_2Ti_2O_7$ irradiated by 1 MeV Kr^+ at room temperature is ~0.18 dpa [2]. This dose is equivalent to a cumulative dose of 4×10^{18} alpha-decays/g or 600 years of storage for waste forms containing 10 wt% ^{239}Pu. The critical amorphization dose (converted to dpa) for U- and Nb-titanates (~0.11 dpa) is of the same order of magnitude as that of $Gd_2Ti_2O_7$ at room temperature.

3.3. Formation of nanocrystals

During the irradiation at 933 K, initially diffraction spots in the SAD from the crystalline material faded gradually. After an ion dose of 6.25×10^{17} ions/m^2, strong arcing of diffraction maxima and polycrystalline rings appeared in the SAD pattern. Nanocrystals, which were irradiation-resistant, were formed in the irradiated specimen. Fig. 6 shows the microstructure and SAD pattern of the U-rich titanate irradiated at 933 K with an ion dose of 2.5×10^{19} ions/m^2. The nanocrystals have a rounded morphology with an average size of ~15 nm (as compared with the original grain size of several μm

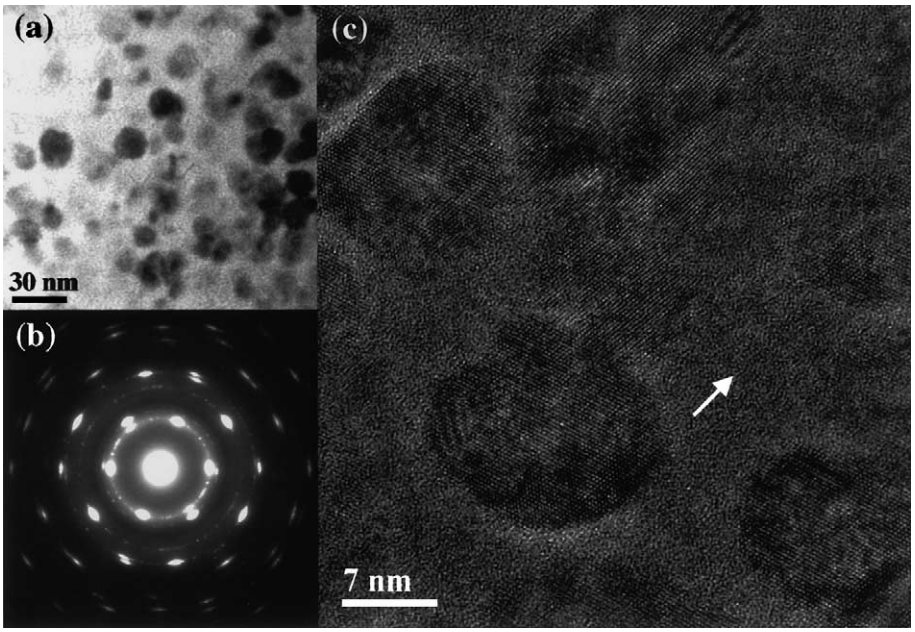

Fig. 6. (a) Bright-field image; (b) SAD pattern; (c) HRTEM image of the U-rich titanate irradiated by 800 keV Kr^{2+} at 933 K. The region marked by the white arrow may be amorphous or contains randomly oriented nanocrystals.

shown in Fig. 1(a)) and are distributed randomly within the substrate. Based on indexing the polycrystalline rings in the SAD pattern, the nanocrystals have the same structure as the original phase. The HRTEM image (Fig. 6(c)) illustrates that some nanocrystals have the same orientation. A few dim diffuse diffraction haloes were observed in the diffraction pattern (Fig. 6(b)) that result from the amorphous regions marked by an arrow between nanocrystals of the same orientation (Fig. 6(c)). Furthermore, some residual crystallites or newly nucleated nanocrystallites with a random orientation could be embedded in these amorphous regions. The different orientations of these crystallites under varying imaging conditions make it difficult to observe the lattice fringes in all of the nanocrystals.

Fig. 7(a) shows a bright-field image of the U-rich titanate irradiated by 800 keV Kr^{2+} at 973 K at an ion dose of 1.88×10^{19} ions/m^2. Nanocrystals also formed under this condition. The dark-field image (Fig. 7(b)) was taken by inserting the objective aperture marked by a circle to cover the diffraction arcing in the SAD. Many nanocrystals showing white contrast were observed in the dark-field image. Moíre fringes, resulting from the interference between different crystals, were observed. The HRTEM image (Fig. 7(c)) shows nanocrystals with a random orientation. The polycrystalline rings in the diffraction pattern inset in Fig. 7(b) also indicate that the orientation of the nanocrystals is completely random. In contrast, most of the nanocrystals in the sample irradiated at 933 K are generally in the same orientation.

The formation of nanocrystals has been observed in many synthetic materials irradiated by energetic ions and in some natural materials that have suffered alpha-decay damage over geologic time [37–39]. Ion irradiation-induced nanocrystallization results from competition between the formation of amorphous domains and crystal recovery [37–42]. The simultaneous recovery processes are mainly associated with epitaxial recrystallization at the crystalline/amorphous interface and nucleation-growth recrystallization in the bulk of the amorphous volume [30].

With epitaxial recrystallization, the displaced atoms within the highly disordered zone created by the incident energetic ions recystallize at the interface of crystalline/amorphous region, and nucleation is not required. Studies [38,39] have suggested that ion irradiation-induced nanocrystallization occurs at temperatures near the critical amorphization temperature, T_c, which is below the thermal recrystallization temperature. Ion irradiation-induced point defects may lower the energy barrier for the phase transformation due to ion irradiation-enhanced diffusion [43]. Meldrum et al. [41] have estimated that the diffusion coefficient necessary to cause solute segregation within the displacement cascade is $D \approx 1 \times 10^{-8}$ m^2/s, which is similar to typical diffusion coefficients in liquids. Thus, the energy barrier for epitaxial recrystallization is less than that of purely thermal recrystallization from an amorphous substrate. Due to the lower activation energy, epitaxial recrystallization dominates the recovery process and occurs simulta-

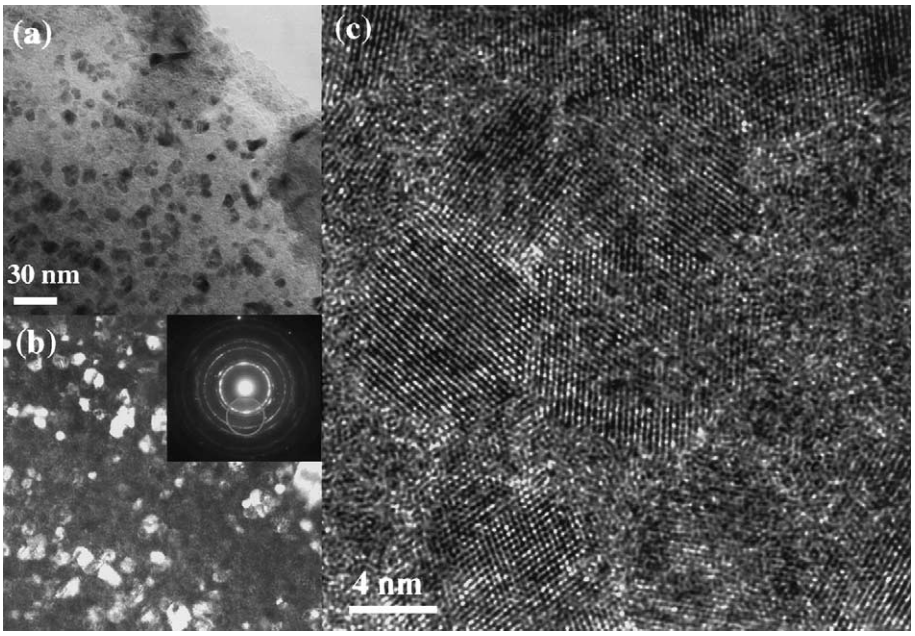

Fig. 7. (a) Bright-field image of the U-rich titanate irradiated by 800 keV Kr^{2+} at 973 K; (b) Dark-field image taken by inserting an objective aperture marked by a circle into SAD pattern; (c) HRTEM of nanocrystals showing random orientation of nanocrystals.

neously with the ion irradiation-induced amorphization process.

During irradiation, some crystalline nuclei may form due to variations in the local concentration of point defects within the highly disordered zones. When these nuclei exceed a critical size, they grow to reduce the free energy and become nuclei for recrystallization. The probability of forming new nuclei that exceed the critical size depends on the nucleation activation energy and temperature. Ion irradiation-induced nucleation and growth has been described as a process that is similar to recrystallization in cold-worked metals for which materials are severely deformed and a high density of defects is created [37,38,44]. In the cold-worked metal, new grains nucleate at or near the subgrain boundaries in the highly deformed materials upon annealing. The larger the degree of deformation, the lower the temperature required for recrystallization. Also, the probability of nucleation increases with longer annealing times and higher temperatures [45].

Under high temperature irradiation (933 K), point defects have a high mobility due to irradiation-enhanced diffusion and thermal annealing. This leads to rapid defect recovery of amorphous regions along the crystalline/amorphous interface. Nanocrystals can be formed due to the epitaxial recrystallization of displaced atoms around the undamaged crystalline nuclei and have a orientation similar to that of the undamaged crystalline nuclei, which are the same as that of the crystalline matrix. In some cases, the local anisotropic strain field induced by the formation of nanocrystals and amorphous volumes may cause a slight rotation of nanocrystals relative to that of the original crystallites; thus, some nanocrystals have a slightly aligned orientation, which contributes to the diffraction arcing in SAD pattern. The polycrystalline rings in the diffraction pattern (Fig. 6(b)) are a result of the contribution of nanocrystals that have random orientations relative to the crystalline matrix. These random nanocrystals can form within the amorphous regions if the recrystallization rate for nucleation-growth is great enough. However, due to the lower activation energy of epitaxial recrystallization (a heterogeneous mechanism), as compared with that of nucleation-growth recrystallization (homogenous), epitaxial recrystallization dominates the formation of the nanocrystals.

At temperatures greater than 973 K, the 'quench' rate for the damage cascade is slower. The probability of nucleation and recrystallization increases with the higher ambient temperature and higher mobility of displaced atoms. Random nanocrystals, as shown in Fig. 7(c), may grow around these newly formed nuclei and contribute to the diffraction rings in the SAD pattern which are characteristic of a polycrystalline material. Under these conditions, ion irradiation-induced nucleation-growth of nanocrystals in heavily damaged crystalline materials at elevated temperature is similar to the thermally activated recrystallization that occurs in cold-worked metals. Thus, epitaxial growth and ion irradiation-induced

nucleation-growth both play important roles in the formation of nanocrystals.

4. Conclusions

Two complex uranium–niobium titanates synthesized by alkoxide/nitrate route at 1300°C under argon atmosphere were analyzed by TEM, EDS, BSE, XRD and EMPA techniques. Three phases coexist including $U_3NbO_{9.8}$ (U-rich titanate), Nb_3UO_{10} (Nb-rich titanate) and rutile.

A 800 keV Kr^{2+} irradiation of these uranium–niobium titanates was performed using the IVEM-Tandem Facility at Argonne National Laboratory from 30 to 973 K. The temperature dependence of the critical amorphization dose was determined by in situ TEM observation. At room temperature, the critical amorphization doses of U-rich titanate and Nb-rich titanate irradiated by 800 keV Kr^{2+} are 4.72×10^{17} and 5×10^{17} ions/m^2, respectively. With an increase in temperature, the critical amorphization dose increased as a result of dynamic annealing. No significant difference of critical amorphization dose was observed between the U-rich and Nb-rich titanates. The critical amorphization temperature for both Nb-rich and U-rich phases is ~930 K. Based on the critical amorphization temperature and critical amorphization dose at room temperature, U-rich and Nb-rich titanates are similarly susceptible to ion irradiation-induced damage as $Gd_2Ti_2O_7$ pyrochlore and $U_2Ti_2O_6$ brannerite.

Above the critical amorphization temperature, complete amorphization cannot occur, and the formation of nanocrystals was observed. The formation of nanocrystals can be attributed to the recrystallization process dominating over amorphization at high temperatures. At 933 K, epitaxial recrystallization dominates, leading to the formation of nanocrystals; whereas, at a higher temperature, both epitaxial growth and ion irradiation-induced nucleation-growth contribute to the formation of nanocrystals.

Acknowledgements

Many thanks to Dr L. Vance at Australian Nuclear Science and Technology Organisation (ANSTO) for supplying the specimen used in this study. The authors also thank the staff of IVEM-Tandem Facility at Argonne National Laboratory for assistance during ion irradiation experiments. HRTEM was conducted at the Electron Microbeam Analysis Laboratory (EMAL) at the University of Michigan. This work was supported by the Office of Basic Energy Sciences, US Department of Energy under grant DE-FG02-97ER45656.

References

[1] W.J. Weber, R.C. Ewing, C.R.A. Catlow et al., J. Mater. Res. 13 (1998) 1434.
[2] W.J. Weber, R.C. Ewing, Science 289 (2000) 2051.
[3] I.W. Donald, B.L. Metcalfe, R.N.J. Taylor, J. Mater. Sci. 32 (1997) 5851.
[4] G.R. Lumpkin, K.P. Hart, P.J. McGlinn, T.E. Payne, Radiochim. Acta 66&67 (1994) 469.
[5] E.R. Vance, Mater. Res. Soc. Bull 19 (1994) 28.
[6] R.C. Ewing, W.J. Weber, W. Lutze, in: E.R. Merz, C.E. Walter (Eds.), Disposal of Weapon Plutonium, Kluwer Academic, Boston, MA, 1996, p. 65.
[7] M.A. Subramanian, G. Aravamudan, G.V. Subba Rao, Prog. Solid State Chem. 15 (1983) 55.
[8] B.C. Chakoumakos, R.C. Ewing, Mater. Res. Soc. Symp. 44 (1985) 641.
[9] A. Jostsons, L. Vance, B. Ebbinghaus, in: Proceedings of the International Conference on Future Nuclear Systems, Global's 99 Nuclear Technology – Bridging the Millennia, Wyoming, 1999.
[10] B.D. Begg, R.A. Day, A. Brownscombe, in: K. Hart, (Ed.), 24th International Symposium on the Scientific Basis for Nuclear Waste Management, Sydney, 2000, in press.
[11] W.J. Weber, J.W. Wald, Hj. Matzke, Mater. Lett. 3 (1985) 173.
[12] W.J. Weber, J.W. Wald, Hj. Matzke, J. Nucl. Mater. 138 (1986) 196.
[13] S.X. Wang, L.M. Wang, R.C. Ewing, G.S. Was, G.R. Lumpkin, Nucl. Instrum. and Meth. B 148 (1999) 704.
[14] S.X. Wang, B.D. Begg, L.M. Wang, R.C. Ewing, W.J. Weber, J. Mater. Res. 14 (1999) 4470.
[15] K.L. Smith, N.J. Zaluzec, G.R. Lumpkin, J. Nucl. Mater. 250 (1997) 36.
[16] R.C. Ewing, L.M. Wang, Nucl. Instrum. and Meth. B 65 (1992) 324.
[17] A.E. Ringwood, S.E. Kesson, N.G. Ware, W. Hibberson, A. Major, Nature 278 (1979) 219.
[18] J.T. Szymanski, J.D. Scott, Can. Mineral. 20 (1982) 271.
[19] A. Pabst, Am. Mineral. 39 (1954) 109.
[20] E.R. Vance, personal communication.
[21] E.R. Vance, Y.J. Zhang, J.N. Watson, K.P. Hart, R.A. Day, B.D. Begg, G.R. Lumpkin, Abstr. Pap. Am. Chem. 219 (2) (2000) 140.
[22] G.R. Lumpkin, K.L. Smith, M.G. Blackford, J. Nucl. Mater. 277 (2001) 177.
[23] J. Lian, L.M. Wang, G.R. Lumpkin, R.C. Ewing, Mater. Res. Soc. Symp. Proc. 650 (2001) R3.17.1.
[24] L.M. Wang, R.C. Ewing, Mater. Res. Soc. Bull. 17 (1992) 238.
[25] L.M. Kovba, E.I. Sirotkina, V.K. Trunov, J. Inorg. Chem. 10 (1965) 138.
[26] S.H. Wang, L.M. Kovba, V.I. Spitsyn, Zh. Strukt. Khim. 4 (1961) 714.
[27] PDF #19-1378, JCPDS, International Centre for Diffraction DTA, 1988, USA.
[28] PDF #31-1414, JCPDS, International Centre for Diffraction DTA, 1979, USA.
[29] E.A. Ippolitova, Y.P. Simanov, L.M. Kovba, G.P. Polunina, I.A. Bereznikova, Radiokhimiya 1 (1959) 660.
[30] W.J. Weber, Nucl. Instrum. and Meth. B 166 (2000) 98.

[31] J.F. Gibbons, Proc. IEEE 60 (1972) 1062.
[32] W.J. Weber, R.C. Ewing, L.M. Wang, J. Mater. Res. 9 (1994) 688.
[33] W.J. Weber, J. Mater. Res. 5 (1990) 2686.
[34] S.X. Wang, L.M. Wang, R.C. Ewing, R.H. Doremus, J. Non-Cryst. Solids 238 (1998) 214.
[35] S.X. Wang, L.M. Wang, R.C. Ewing, R.H. Doremus, J. Non-Cryst. Solids 238 (1998) 198.
[36] S.X. Wang, L.M. Wang, R.C. Ewing, Phys. Rev. B 63 (2001) 024,105.
[37] L.M. Wang, S.X. Wang, R.C. Ewing, A. Meldrum, R.C. Birtcher, P.N. Provencio, W.J. Weber, Hj. Matzke, Mater. Sci. Eng. A 286 (2000) 72.
[38] L.M. Wang, R.C. Birtcher, R.C. Ewing, Nucl. Instrum. and Meth. B 80&81 (1993) 1109.
[39] R.C. Birtcher, L.M. Wang, Nucl. Instrum. and Meth. B 59–61 (1991) 966.
[40] A. Meldrum, L.A. Boatner, S.J. Zinkle, S.X. Wang, L.M. Wang, R.C. Ewing, Can. Mineral. 37 (1999) 207.
[41] A. Meldrum, S.J. Zinkle, L.A. Boatner, R.C. Ewing, Nature 395 (1998) 56.
[42] A. Meldrum, L.A. Boatner, C.W. White, D.O. Henderson, Mater. Res. Soc. Symp. Proc. 540 (1999) 135.
[43] Y. Bar-Yam, T.D. Moustakas, Nature 342 (1989) 786.
[44] L.M. Wang, W.J. Weber, Philos. Mag. A 79 (1999) 237.
[45] R.W. Cahn, P. Haasen (Eds.), Physical Metallurgy, Elsevier, Amsterdam, 1983.